J. Fluid Mech. (2013), *vol.* 717, *pp.* 293–321.
doi:10.1017/jfm.2012.573

Reynolds- and Mach-number effects in canonical shock–turbulence interaction

Johan Larsson†, Ivan Bermejo-Moreno and Sanjiva K. Lele

Center for Turbulence Research, Stanford University, Stanford, CA 94305, USA

(Received 22 June 2012; revised 5 November 2012; accepted 18 November 2012;
first published online 1 February 2013)

The interaction between isotropic turbulence and a normal shock wave is investigated through a series of direct numerical simulations at different Reynolds numbers and mean and turbulent Mach numbers. The computed data are compared to experiments and linear theory, showing that the amplification of turbulence kinetic energy across a shock wave is described well using linearized dynamics. The post-shock anisotropy of the turbulence, however, is qualitatively different from that predicted by linear analysis. The jumps in mean density and pressure are lower than the non-turbulent Rankine–Hugoniot results by a factor of the square of the turbulence intensity. It is shown that the dissipative scales of turbulence return to isotropy within about 10 convected Kolmogorov time scales, a distance that becomes very small at high Reynolds numbers. Special attention is paid to the 'broken shock' regime of intense turbulence, where the shock can be locally replaced by smooth compressions. Grid convergence of the probability density function of the shock jumps proves that this effect is physical, and not an artefact of the numerical scheme.

Key words: compressible turbulence, shock waves, turbulent flows

1. Introduction

The interaction of turbulence with a shock wave is a fundamental problem in fluid mechanics, with relevance to a wide range of fields and applications including aeronautics (supersonic flight and propulsion), astrophysics (supernovae explosions, accretion shocks), nuclear physics (inertial confinement fusion) and medicine (shock wave lithotripsy). The canonical shock–turbulence interaction problem, where additional complications (e.g. mean shear, streamline curvature, real gas effects, magnetic effects, etc.) have been removed, is that of isotropic turbulence passing through a nominally planar shock wave. This canonical problem is the focus of the present study.

Figure 1 shows the essence of the canonical shock–turbulence interaction. Isotropic turbulence, characterized by a Taylor-scale Reynolds number Re_λ and a turbulent Mach number M_t, passes through a normal shock wave, characterized by the mean

† Present address: Department of Mechanical Engineering, University of Maryland, College Park, MD 20742, USA. Email address for correspondence: jola@umd.edu

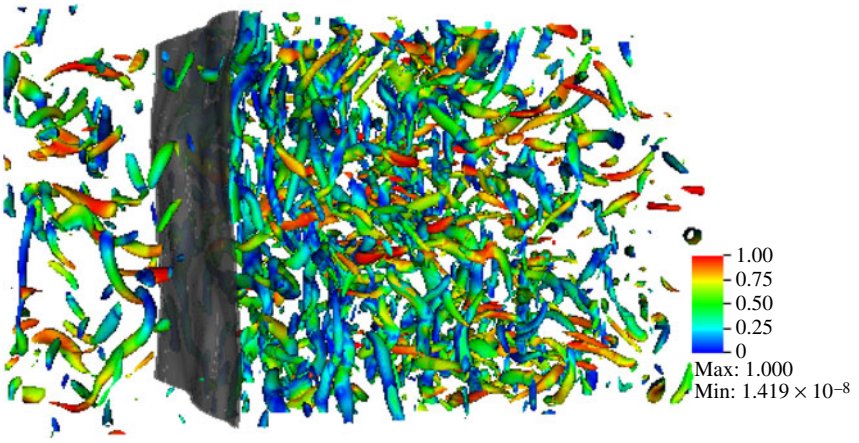

FIGURE 1. (Colour online) Snapshot of eddies extracted by the Q-criterion and shaded/coloured by the cosine of the angle between the vorticity vector and the shock-normal direction. The shock is visualized by an isosurface at large negative dilatation, and the flow is from left to right.

Mach number M. The initially isotropic turbulence becomes compressed, energized and anisotropic as it passes through the shock. The figure clearly shows that most post-shock eddies immediately behind the shock are oriented in the plane of the shock; some distance downstream of the shock, the orientation of the eddies becomes more isotropic again.

Theoretical studies based on the mode decomposition of turbulence in supersonic flows (Kovasznay 1953) were first developed in Ribner's linear analysis (Ribner 1953, 1954). Lele (1992) combined rapid distortion theory (RDT) with gas dynamics to formulate the jump relations across a shock in a turbulent mean flow, whereas Jacquin, Cambon & Blin (1993) used RDT and Helmholtz's decomposition of the fluctuating field to obtain two regimes (solenoidal acoustic and 'pressure-released'), thus limiting the amplification of turbulent kinetic energy that occurs when the fluid is processed by the shock. RDT incorporates more restrictive assumptions than does the broader linear interaction analysis, resulting in its more limited scope and agreement with experiments. By using recently developed analytical techniques, Wouchuk, Huete Ruiz de Lira & Velikovich (2009) constructed an exact analytical model of the shock–turbulence interaction, obtaining closed-form expressions for several quantities of interest. More recently, Donzis (2012*a*) approached the problem from a different direction, by using dimensional and similarity arguments to argue that both the amplification of the shock-normal Reynolds stress and whether the interaction is in the 'broken shock' or 'wrinkled shock' regimes (to be defined below) should scale with $M_t/[\sqrt{Re_\lambda}(M-1)]$. This is in contrast to Ribner's linear theory, which is valid only in the limits of large Re_λ and small M_t. In follow-up work, Donzis (2012*b*) then expanded and deepened the analysis to make theoretical predictions regarding the structure of the shock in the presence of turbulence.

Experiments have been carried out in shock tubes and wind tunnels with different means of generating turbulence. Hesselink & Sturtevant (1988) considered the propagation of weak shocks in a random medium and explained the wave front distortion they encountered in terms of medium inhomogeneities that focus/defocus the front. Keller & Merzkirch (1990) used a shock tube with grid-generated turbulence and

a shock wave reflecting at the end wall; they saw amplification of turbulence occurring at larger scales, but not at the small-scale structures. Barre, Alem & Bonnet (1996) studied, with hot-wire and laser Doppler velocimetry (LDV) techniques, the interaction in a wind tunnel of a normal shock and quasi-homogeneous isotropic turbulence generated using a multi-nozzle in a Mach 3 flow. They found close agreement with Ribner's linear theory for the amplification of velocity fluctuations, and some discrepancy with earlier experiments for the turbulent energy amplification present at low wavenumbers. In an experiment by Agui, Briassulis & Andreopoulos (2005), an incident shock generated an induced flow behind it that passed later through a grid to obtain a nearly homogeneous and isotropic flow field, which was then processed by the reflected shock. Intense vorticity structures were suggested as the cause of high-amplitude events of time signals of enstrophy, dissipation rate and dilatational stretching; the dissipation seemed to have a more dominant effect on the flow motions than on the enstrophy.

Direct numerical simulations (DNS) of the shock–turbulence interaction problem have emerged in the literature over the past couple of decades. Lee, Lele & Moin (1993) (see also Lee, Lele & Moin 1994) found partial agreement with linear analysis, with some discrepancy arising as the turbulent Mach number, M_t, was increased, resulting in distorted shock waves lacking a well-defined front. This work was later extended to stronger shocks (Lee, Lele & Moin 1997). Hannappel & Friedrich (1995) related the amplification of turbulent kinetic energy to the ratio of compressible to incompressible kinetic energy, explaining the different behaviour in terms of the pressure diffusion term of the turbulent kinetic energy equation. Mahesh, Lele & Moin (1997) found that upstream correlations of vorticity–entropy and velocity–temperature fluctuations have a strong influence on the turbulence evolution across the shock. Jamme *et al.* (2002) studied the effect of different types of isotropic turbulence (by combining entropy, vortical and acoustic fluctuations), and reported their influence in the amplification of kinetic energy and vorticity variance, as well as in the reduction of the transverse microscale. Their results agreed well with linear analysis. Sesterhenn, Dohogne & Friedrich (2005) used a shock-fitting algorithm that provided good agreement with the more widely used shock-capturing methods.

In the DNS of Larsson & Lele (2009), the small scales where viscous dissipation occurs were shown to decrease significantly in size during the interaction with the shock, implying that the resolution requirements behind the shock are substantially finer than before it. This insight combined with a grid convergence study allowed for the viscous dissipation to be fully resolved immediately behind the shock. The amplification of turbulence kinetic energy (TKE) was observed to agree well with the predictions of linear theory, while the turbulence anisotropy and Taylor length scales showed qualitative disagreements between DNS and linear theory. Moreover, this study identified two different regimes of the interaction depending on the strength of the incoming turbulence: the 'wrinkled shock' regime in which the shock retains its topological structure, and the 'broken shock' regime in which it does not (e.g. where the shock is locally, in space and time, replaced by a smooth compression or by multiple weaker shocks). Finally, Grube, Taylor & Pino Martín (2011) considered highly compressible turbulence with much higher turbulent Mach number than in previous studies ($M_t \gtrsim 0.7$ compared to $M_t \lesssim 0.4$ in the studies mentioned above), where the incoming turbulence spontaneously generates eddy shocklets. They found general agreement with results using less compressible incoming turbulence (without eddy shocklets).

The present study builds on our prior work reported in Larsson & Lele (2009), with deeper analysis and post-processing of the DNS databases. Additionally, new simulations at higher Reynolds number have been performed, allowing for an assessment of the effect of Re on the interaction. The study focuses primarily on two different aspects of the shock–turbulence interaction problem: (i) the amplification of turbulence and how this compares to linear theory; and (ii) how the turbulence modifies the shock and how this scales with the flow parameters. Finally, to encourage and enable deeper and novel analysis of these DNS databases, both comprehensive statistics and the raw databases are available for download from the corresponding author.

The paper is organized as follows. The numerical method and simulation parameters are described in § 2, along with verification of the quality of the computed data. This material naturally lends itself to discussing certain physical effects as well, including the post-shock Kolmogorov scale and the mean shock jumps. The behaviour of the Reynolds stresses and vorticity variances is discussed in § 3, along with validation using experimental data and comparison to the predictions of linear theory. Finally, the different interaction regimes are discussed in § 4, including some visualization of instantaneous flow fields.

2. Methodology and verification

The compressible Navier–Stokes equations for a perfect gas are solved using DNS. The density, velocity, pressure and temperature are denoted by ρ, u_i, p and T, respectively. The ratio of specific heats is $\gamma = c_p/c_v = 1.4$, and the viscosity is approximated by a power law $\mu = \mu_{ref}\,(T/T_{ref})^{3/4}$. The spatial coordinates are x_i, where x_1 is the shock-normal (streamwise) direction. The shock is located at $x_1 = 0$ on average. Averages are computed over the homogeneous x_2 and x_3 directions and over time t. Standard (Reynolds) averages are denoted by an overbar, $\overline{f}$, while density-weighted (Favre) averages are denoted by a tilde, $\widetilde{f} = \overline{\rho f}/\overline{\rho}$; fluctuations around these averages are denoted by single and double primes, as $f' = f - \overline{f}$ and $f'' = f - \widetilde{f}$, respectively. The Reynolds stresses are $R_{ij} \equiv \widetilde{u_i'' u_j''}$. Given the axisymmetric nature of this problem, the off-diagonal stresses are naturally zero.

Reference values are taken from immediately upstream of the shock and denoted by subscript 'u'; downstream, post-shock values are denoted by subscript 'd'. We can then define the mean Mach number $M = \widetilde{u}_{1,u}/\widetilde{c}_u$ and the turbulent Mach number $M_t = \sqrt{R_{kk}}/\widetilde{c}_u$. We consider two different Reynolds numbers, based on the dissipation length scale $L_\varepsilon = (R_{kk}/2)^{3/2}/\varepsilon$ and on the Taylor length scale λ, where $\lambda^2 = R_{22}/\overline{(\partial_2 u_2)^2}$ and ε is the dissipation rate of TKE; these Reynolds numbers are $Re_L = \overline{\rho}\sqrt{R_{kk}/3}\,L_\varepsilon/\overline{\mu}$ and $Re_\lambda = \overline{\rho}\sqrt{R_{kk}/3}\,\lambda/\overline{\mu}$, respectively (where all quantities are taken immediately upstream of the shock).

The present study uses DNS in the extended sense that all scales of turbulence are computed but the shock waves are captured numerically. This approach inherently relies on the assumption of a separation of length scales associated with those two physical phenomena: if the smallest eddies (of size comparable to the Kolmogorov length scale, η) are much larger than the physical thickness of the shock, δ_s, then the shock essentially represents a discontinuity to the turbulent eddies. Hence, the shock–turbulence interaction process is accurately described provided that the numerical shock thickness, δ_n, is sufficiently small compared to η. This has been verified in several prior studies, using different methods: Lee *et al.* (1997) compared

shock-resolved simulations (where the viscous shock profile was resolved) with shock-captured simulations (where it was not), and found excellent agreement. A different approach was taken in Larsson (2010), where a theoretical model of the error introduced by the numerical shock-capturing was used to predict and quantify the error on the post-shock turbulence. The error in post-shock second-order statistics was found to scale as the square of the shock-normal grid spacing; this was also confirmed in numerical experiments. Quantitatively, this study concluded that the shock-capturing error in DNS is negligible except at very low Reynolds numbers. The final verification of the extended DNS methodology is through standard grid refinement to verify that all computed statistics are insensitive to the grid spacing. This verification is shown in § 2.1 for the present work.

A solution-adaptive finite-difference method (Larsson & Lele 2009) that applies different numerical schemes to shocks and broadband turbulence is utilized, the idea being to use numerics that are well suited to each physical phenomenon. Narrow regions around shock waves are treated with a fifth-order accurate weighted essentially non-oscillatory (WENO) scheme with Roe flux splitting, whereas a sixth-order accurate central difference scheme in the split form by Ducros *et al.* (2000) is used in the remainder of the domain. The use of the split form drastically improves nonlinear numerical stability, and no de-aliasing filter is used. During each time step, shock waves are identified as regions where the negative dilatation is greater than the low-pass-filtered vorticity magnitude, i.e. where $-\partial_k u_k > \sqrt{\omega_k \omega_k}$, with $\omega_i = \epsilon_{ijk}\partial_j u_k$ being the vorticity. Having identified the grid points occupied by shock waves, the WENO scheme is applied to the narrow region comprising those points as well as three additional grid points in every direction in order to ensure that the central scheme is never used across any shocks. The switching between different numerical schemes introduces internal 'interfaces' in the domain. The method devised by Pirozzoli (2002) is used to ensure conservation across these interfaces, and the numerical stability of the interfaces has been analysed and verified (Larsson & Gustafsson 2008). Time advancement is done using a fourth-order accurate explicit Runge–Kutta scheme.

The numerical method has been verified and validated on several problems (cf. Johnsen *et al.* 2010), including the canonical shock–turbulence interaction problem (Larsson & Lele 2009). We specifically note that the solution-adaptive method has no effect on the results: grid convergence tests (§ 2.1) show that the numerical errors are negligibly small, and many separate tests (some of which are reported in Johnsen *et al.* (2010)) have confirmed that the switching between different schemes has no discernible impact on the results, provided sufficient grid resolution.

The specification of inflow turbulence from pre-computed periodic boxes of isotropic turbulence is described in Larsson & Lele (2009); briefly, isotropic turbulence was allowed to decay temporally until the turbulence was deemed developed, as judged by having decaying vorticity variance and a velocity derivative skewness settled around -0.5. These measures are both related to the small scales, whereas the larger scales develop more slowly (especially at higher Reynolds numbers). Therefore, the cases at the higher Reynolds number were allowed to decay for a longer time, specifically until the dissipation length scale L_ε had started growing in time. Finally, multiple independent boxes were blended together using the technique described in Larsson (2009).

A total of 20 cases have been computed, all of which are listed in table 1. The first 16 cases are at $Re_\lambda \approx 40$ with $Re_L \approx 200$, while the final four cases are at $Re_\lambda \approx 70$ with $Re_L \approx 650$. A third measure of the turbulence Reynolds number, the ratio of the dissipation length scale to the Kolmogorov scale, is also listed in the

Re_λ	Re_L	L_ε/η	M	M_t	Grid	$\Delta x_{2,3}/\Delta x_{1,s}$
39	180	58	1.05	0.05	828×384^2	1.3
38	180	57	1.28	0.15	1040×384^2	2.0
39	190	59	1.28	0.22	1040×384^2	2.0
38	180	57	1.28	0.26	1040×384^2	2.0
38	180	57	1.28	0.31	1040×384^2	2.0
38	180	57	1.50	0.15	1040×384^2	2.0
39	190	59	1.50	0.22	1040×384^2	2.0
39	190	59	1.51	0.31	1040×384^2	2.0
39	180	58	1.51	0.37	1040×384^2	2.0
39	190	59	1.87	0.22	1040×384^2	2.0
39	190	59	1.87	0.31	1040×384^2	2.0
40	200	61	2.50	0.22	1257×384^2	2.8
40	200	62	3.50	0.16	1257×384^2	2.8
41	210	63	3.50	0.23	1257×384^2	2.8
42	210	65	4.70	0.23	1257×384^2	2.8
42	220	66	6.00	0.23	1257×384^2	2.8
73	650	149	1.50	0.14	2234×1024^2	2.8
73	660	152	1.50	0.22	2234×1024^2	2.8
72	650	150	1.52	0.38	2366×1024^2	2.8
74	670	153	3.50	0.15	2234×1024^2	2.8

TABLE 1. List of cases in the present study with parameters taken immediately upstream of the shock.

table; this measure is about 60 and 150 at the two different Reynolds numbers, respectively. The low- and high-*Re* cases use grids with 384 and 1024 points in the transverse directions, respectively. The grid is stretched in the shock-normal direction such that the grid spacing $\Delta x_{1,s}$ at and immediately behind the shock is appropriate for the anisotropically compressed post-shock turbulence. This reduced shock-normal grid spacing also minimizes the numerical error incurred at and immediately behind the shock, to the point where this error is negligible according to the analysis and criteria given by Larsson (2010). This grid stretching implies that the number of points in the shock-normal direction differs between the cases. The simulations were run on 4096–65 536 cores for about 6–18 h depending on the case.

In the following sections the quality of the computed data is assessed. The material also lends itself naturally to discuss some physical phenomena, including the decrease of the Kolmogorov scale at the shock.

When presenting data, it is natural to normalize by the conditions immediately upstream of the shock. What is less clear is how to scale the shock-normal coordinate, i.e. what the relevant length scale is. One choice is a characteristic eddy size, which could be either the dissipation length scale L_ε or the Kolmogorov length scale η for the large and small motions, respectively. Another choice is a convected time scale characteristic of the evolution of turbulence, which could be taken as $\widetilde{u}\tau_\varepsilon = \widetilde{u}(R_{kk}/2)/\varepsilon$ or $\widetilde{u}\tau_\eta = \widetilde{u}\sqrt{\nu/\varepsilon}$ for the large and small scales, respectively.

2.1. *Grid convergence and decrease of the Kolmogorov scale*

The most basic test of the quality of DNS data is to verify that the statistics are grid converged. Figure 2 shows the shock-normal Reynolds stress R_{11} and the dissipation rate ε for a sequence of grids at $Re_\lambda \approx 70$. The error in R_{11} is less than 0.1 % on

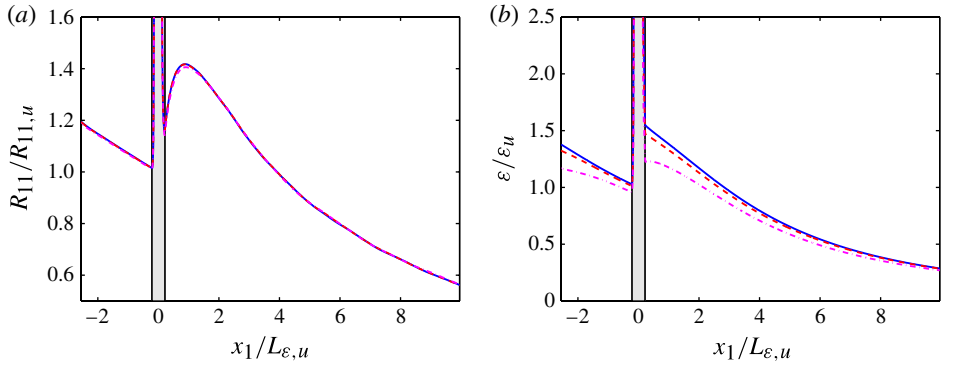

FIGURE 2. (Colour online) Grid convergence at $(M, M_t) = (1.50, 0.14)$ and $Re_\lambda = 73$ on 2234×1024^2 grid (solid), 1675×768^2 grid (dashed) and 1117×512^2 grid (dash-dotted): (*a*) shock-normal Reynolds stress R_{11}; (*b*) dissipation rate ε. Both quantities are normalized by their values upstream of the shock on the finest grid. The grey strip shows the region of unsteady shock movement.

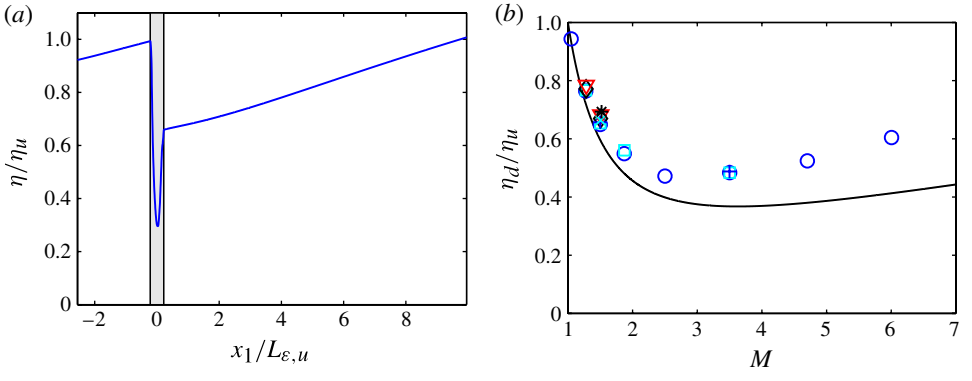

FIGURE 3. (Colour online) Kolmogorov length scale η. (*a*) Profile through the shock at $(M, M_t) = (1.50, 0.14)$ and $Re_\lambda = 73$. The grey strip shows the region of unsteady shock movement. (*b*) Change in η across the shock for all cases versus Mach number. At each Mach number, the cases are shown with different symbols in order of increasing M_t. At $Re_\lambda \approx 40$ the symbols are, in order: circle, square, diamond, and triangle. At $Re_\lambda \approx 70$ the symbols are, in order: plus, cross, and star. The solid line is the estimate from (2.1).

the finest grid, while the error in ε is less than 3 %. That the error in dissipation rate is larger is natural, since it depends primarily on the smallest scales of turbulence (that are the least resolved). The low-Reynolds-number cases at $Re_\lambda \approx 40$ are better resolved, with smaller errors.

The increase in dissipation rate across the shock evident in figure 2 immediately suggests that the Kolmogorov scale also changes across the shock. A sample profile of the Kolmogorov length scale $\eta = \nu^{3/4}\varepsilon^{-1/4}$ is shown in figure 3, which clearly demonstrates this effect. This decrease in η was one of the main points made by Larsson & Lele (2009), who estimated the change as

$$\frac{\eta_d}{\eta_u} \sim \left(\frac{T_d}{T_u}\right)^{3/8} \left(\frac{\rho_d}{\rho_u}\right)^{-1}, \tag{2.1}$$

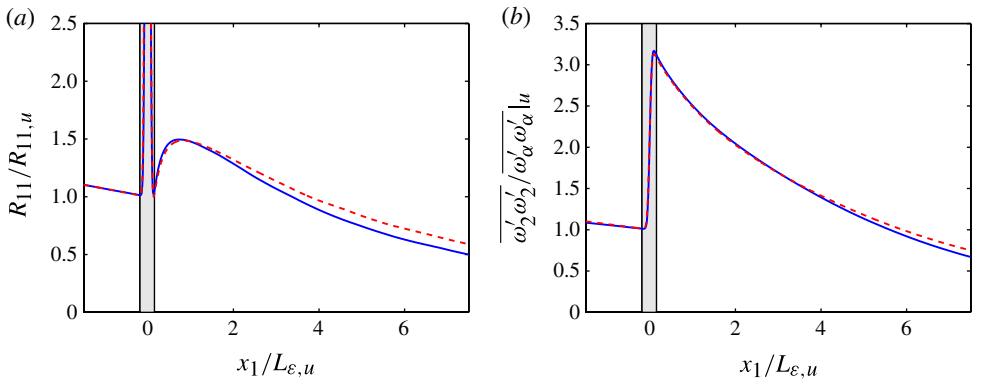

FIGURE 4. (Colour online) Effect of the computational box size. Profiles through the shock at $(M, M_t) = (1.50, 0.15)$ and $Re_\lambda = 38$ of (*a*) R_{11} stress and (*b*) transverse vorticity variance $\overline{\omega_2'\omega_2'}$. Peak energy at the initial time at mode number 4 (solid) and 8 (dashed). The grey strip shows the region of unsteady shock movement.

where the density and temperature jumps are to be taken from the Rankine–Hugoniot relations. The change across the shock of the Kolmogorov length scale is shown in figure 3 for all cases as a function of the Mach number. There is no real effect of either the Reynolds number or the turbulent Mach number on this phenomenon. The agreement with the estimate (2.1) is reasonable but not great, especially at large Mach numbers. The culprit is the simplistic estimate of the vorticity jump across the shock being proportional to the density jump; a better estimate could be developed using more elaborate theory (cf. Sinha 2012). Nevertheless, the estimate captures the main effect of a decrease in η across a shock wave.

We note that the present results for the change in η differ slightly from those reported in Larsson & Lele (2009) as a result of a different definition of the post-shock value η_d: it is defined as the value immediately behind the region of unsteady shock motion (i.e. at the point where the profile leaves the grey strip in figure 3) in the present study.

2.2. *Box size effects and spectra*

The grid convergence in the previous section assesses how well the smallest scales are resolved by the grid; in this section the focus is instead on how the largest scales are affected by the finite computational box size. This test is performed at $Re_\lambda = 38$ for the $(M, M_t) = (1.50, 0.15)$ case. The base case has peak energy at mode number 4 (i.e. at wavenumber 4 in a domain of length 2π) in the inflow database at the initial time. This is compared to a case with peak energy at mode number 8 but all other parameters matched (including the grid spacing in terms of the Kolmogorov scale). Two profiles through the shock are shown in figure 4 for typical large- and small-scale quantities. The results collapse very well except for some discrepancy in the viscous decay region behind the shock. We note that the cases at $Re_\lambda \approx 70$ have peak energy at mode number 6 at the initial time, and therefore are less affected by finite box size effects.

The box size effects are further investigated in figure 5, which shows the spectra of the streamwise velocity u' in the transverse directions. The almost perfect collapse

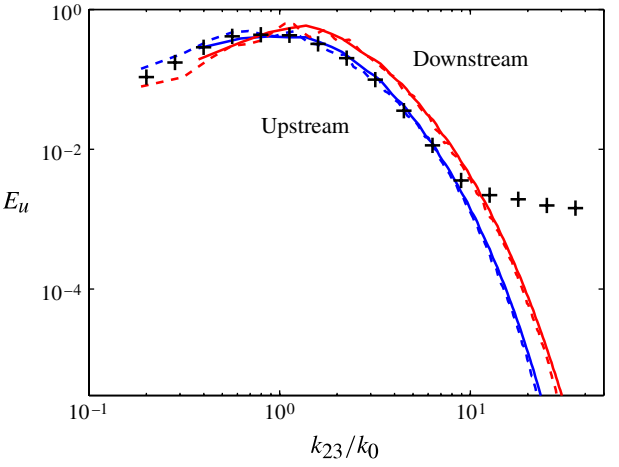

FIGURE 5. (Colour online) Effect of the computational box size. Spectra in the transverse directions (wavenumber $k_{23} = \sqrt{k_2^2 + k_3^2}$) at $(M, M_t) = (1.50, 0.15)$ and $Re_\lambda = 38$ of streamwise velocity u_1 (lines). Peak energy at the initial time at mode number 4 (solid) and 8 (dashed), for positions upstream ($x_1/L_{\varepsilon,u} = -0.5$) and downstream ($x_1/L_{\varepsilon,u} = 0.5$) of the shock. Also shown is the spectrum of the unsteady shock-motion $\dot{x}_s$ (symbols). The spectra have been normalized by their respective variances.

of the spectra for positions both upstream and downstream of the shock again implies that effects of the finite box size are minimal.

Figure 5 also shows the spectrum of the unsteady shock motion $\dot{x}_s$, which is defined as the time derivative of the instantaneous shock location $x_s(x_2, x_3, t)$ (to be defined and discussed in § 4). The spectrum of $\dot{x}_s$ is almost identical to the spectrum of the incoming velocity, suggesting that the shock is forced by the incoming flow. While a rather obvious observation, this will be utilized in § 4.3 to derive a regime criterion for the shock–turbulence interaction process.

2.3. *Shock drift and shock jumps*

In canonical shock–turbulence interaction there are no geometric features anchoring the shock in a particular location, and the shock is free to move in response to the incoming flow. Moreover, the Rankine–Hugoniot relations are valid only for the instantaneous flow, but not on average in the presence of turbulence (Lele 1992). The average shock-jump relations for a turbulent flow include the turbulence stresses and heat flux, which are modified across the shock; therefore, the jumps in the mean quantities are also modified compared to quiescent flow. This effect has a practical importance for computation of canonical shock–turbulence interaction, in that the shock may have a finite and possibly large drift velocity. An example is shown in figure 6, where the instantaneous mean (in the transverse directions) position of the shock is seen to drift in time. There is a clear change in drift velocity at $t/\tau_{db} \approx 4.7$; this time corresponds to the time it takes an acoustic wave to propagate from the outlet to the shock. This process is the slowest of the different initial transients and determines when the problem becomes fully developed. After this transient, the mean drift velocity for the case in the figure is less than 0.2 % of the mean incoming velocity, which is sufficiently small to have negligible effects on the problem (e.g. on

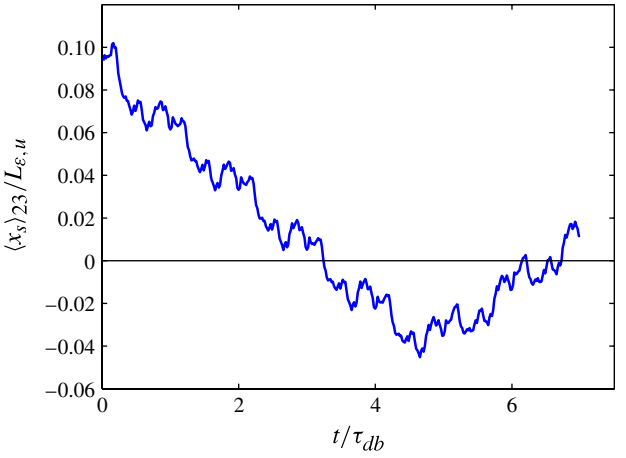

FIGURE 6. (Colour online) Instantaneous mean (in the transverse directions) shock position as a function of time for $(M, M_t) = (1.52, 0.38)$ and $Re_\lambda = 72$. The time is normalized by the duration of the inflow database; averages are collected only during the final τ_{db}. The final drift velocity of the shock is less than 0.2 % of the upstream velocity.

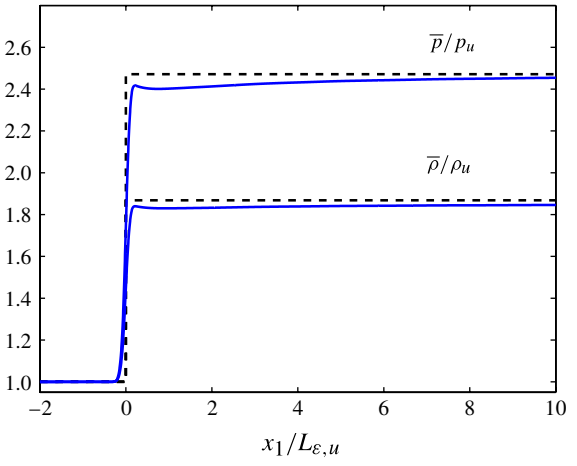

FIGURE 7. (Colour online) Representative mean density and pressure profiles (solid) for $(M, M_t) = (1.50, 0.22)$ and $Re_\lambda = 73$, compared to the inviscid, non-turbulent, Rankine–Hugoniot results (dashed).

the collection of averages). We note that the case in the figure has the largest drift velocity among all cases due to the high turbulence intensity.

As a practical matter, the negligible drift was achieved by utilizing a linearized Rankine–Hugoniot relation for the pressure jump to adjust the specified back-pressure until the shock remained essentially stationary (Larsson & Lele 2009).

Typical profiles of mean density and pressure are shown in figure 7. It is clear that the jumps across the shock are smaller than predicted by the Rankine–Hugoniot relations, in qualitative agreement with the analysis of Lele (1992). To investigate whether there is quantitative agreement with that theory, the deviation from the

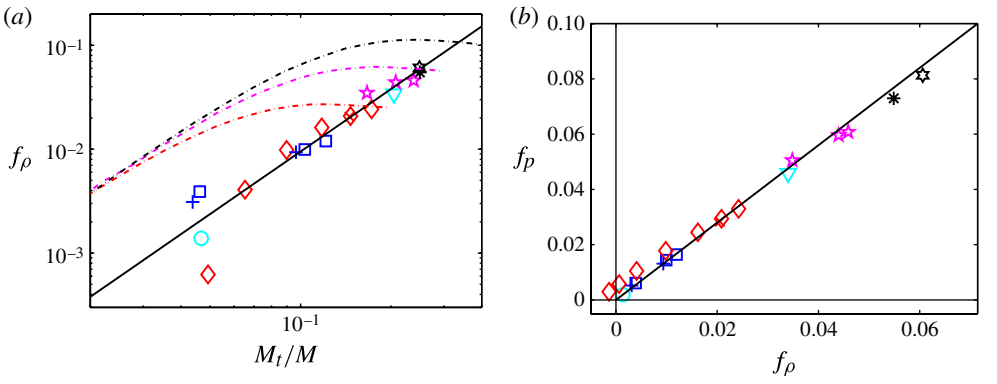

FIGURE 8. (Colour online) Deviation in the mean density and pressure jumps across the shock from the inviscid Rankine–Hugoniot relations, as measured by f_ρ and f_p (defined in the text). (*a*) Deviation in the density jump f_ρ, compared to the empirical fit $f_\rho \approx 0.95\,(M_t/M)^2$ (solid) and the analysis of Lele (1992) (three dash-dotted curves at, from bottom to top, $M_t = 0.2$, 0.3 and 0.4). (*b*) Deviations in pressure f_p versus density f_ρ, compared to the curve $f_p = \gamma f_\rho$ (solid). DNS results at $Re_\lambda \approx 40$ with $M_t \approx 0.05$ (circle), 0.15 (square), 0.22 (diamond), 0.26 (triangle), 0.31 (pentagram) and 0.37 (hexagram). DNS results at $Re_\lambda \approx 70$ with $M_t \approx 0.15$ (plus), 0.22 (cross) and 0.38 (star).

Rankine–Hugoniot jump is defined as

$$f_\rho = \frac{\rho_{d,RH} - \overline{\rho}_d}{\rho_{d,RH}}, \tag{2.2}$$

where subscript *RH* implies the Rankine–Hugoniot value. The deviation in the pressure jump f_p is defined similarly. The post-shock values from the DNS are taken at the local minimum behind the shock, after the inviscid post-shock adjustment. The deviations are shown in figure 8. While the theory of Lele (1992) is qualitatively correct (predicting small positive values of f_ρ), there are quantitative discrepancies with the present DNS data. These discrepancies could perhaps be attributed to the application in Lele (1992) of homogeneous RDT, which is known to have shortcomings for shock–turbulence interaction. The deviation from the Rankine–Hugoniot relations in the DNS data scales rather closely with $(M_t/M)^2$ or, equivalently, with the square of the turbulence intensity upstream of the shock. The deviations in pressure and density are proportional to each other with a factor of γ; in other words, the deviations are isentropic.

Estimates of the deviations f_ρ and f_p from the Rankine–Hugoniot values can be derived by considering the mean conservation equations. Conservation implies that

$$\overline{\rho}\,\widetilde{u}_1 = \text{const.}, \tag{2.3a}$$

$$\overline{\rho}\,\widetilde{u}_1^2 + \overline{p} + [\overline{\rho} R_{11}] = \text{const.}, \tag{2.3b}$$

$$\frac{1}{2}\overline{\rho}\,\widetilde{u}_1^3 + \frac{\gamma}{\gamma - 1}\overline{p}\widetilde{u}_1 + \left[\overline{\rho}\,\widetilde{u}_1\left(R_{11} + \frac{R_{kk}}{2}\right)\right] \approx \text{const.}, \tag{2.3c}$$

where the dominant terms due to turbulence are enclosed in square brackets; the turbulent triple correlation and the temperature–velocity correlation were neglected for simplicity. These jump relations could be combined into turbulent Rankine–Hugoniot relations, and solved provided a closure for the jumps in the turbulence stresses is

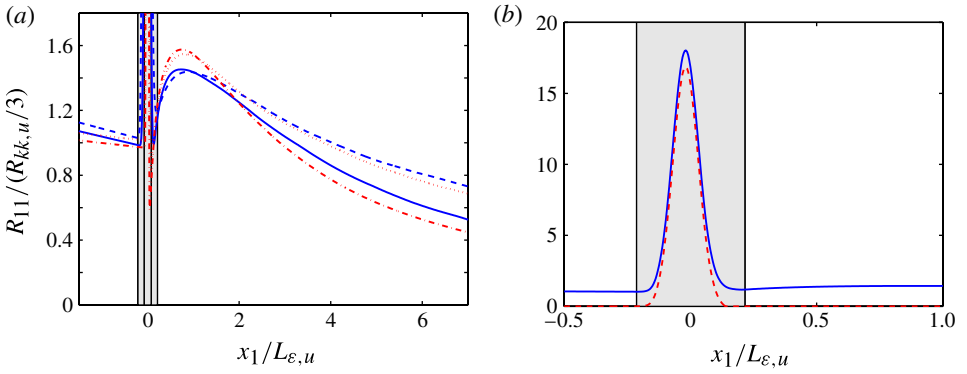

FIGURE 9. (Colour online) Profiles of the shock-normal Reynolds stress R_{11} through the shock at $M_t \approx 0.15$. (*a*) Results at $M = 1.50$ with Re_λ of 38 (solid) and 73 (dashed), respectively, and at $M = 3.50$ with Re_λ of 40 (dash-dotted) and 74 (dotted), respectively. Note that the cases at $M = 1.50$ have the lowest post-shock peak at $x_1/L_{\varepsilon,u} \approx 0.8$, while the cases at $M = 3.50$ have the highest post-shock peak at the same location. (*b*) Zoom around the shock, showing the full peak in R_{11} for $(M, M_t) = (1.50, 0.14)$ and $Re_\lambda = 73$ (solid). Also shown is the estimated profile of R_{11} solely due to the unsteady shock movement (dashed). The grey strips show the regions of unsteady shock movement (in panel (*a*), the narrower region corresponds to $M = 3.50$).

assumed. This was done by Lele (1992) using homogeneous RDT as the closure, but could instead be done using results of Ribner's linear theory to achieve a more accurate closure. However, let us instead simply estimate the scaling of the deviations f_ρ and f_p using (2.3). The non-turbulent terms in (2.3*b*) are of order $\overline{\rho}\,\widetilde{u}_1^2$ while those in (2.3*c*) are of order $\overline{\rho}\,\widetilde{u}_1^3$. The turbulence terms in both equations are therefore of relative magnitudes $R_{11}/\widetilde{u}_1^2$ and $R_{kk}/\widetilde{u}_1^2$; when evaluated upstream of the shock, this is exactly the square of the turbulence intensity, or equivalently $(M_t/M)^2$. Therefore, the deviations $f_{\rho,p}$ should scale, to first order, as $(M_t/M)^2$. In fact, expanding $f_{\rho,p}$ in powers of $(M_t/M)^2$ and solving the jump relations gives $f_\rho/(M_t/M)^2$ of order unity, and f_p/f_ρ close to γ. For both quantities, the exact values are weak functions of M, and, of course, depend on the exact closure used.

3. Reynolds stresses and vorticity

3.1. *Reynolds stresses: evolution through the shock*

Profiles of the shock-normal Reynolds stress R_{11} through the shock are shown in figure 9 for four cases with fixed M_t. The post-shock evolution of R_{11} is non-monotonic, with a clear peak located about 0.8 units of $L_{\varepsilon,u}$ behind the shock location. This peak is a consequence of a post-shock adjustment in which internal energy is converted into shock-normal velocity fluctuations. This adjustment process is predicted by Ribner's linear theory. The main effect of increasing the Reynolds number is a slower decay rate behind the shock. This is not surprising at these low Reynolds numbers. The fact that the post-shock peak, in both magnitude and position, is insensitive to the Reynolds number implies that the post-shock adjustment process is inviscid and occurs primarily at the large scales. The effect of changing the mean Mach number is to modify the amplification of R_{11}, while the position of the peak

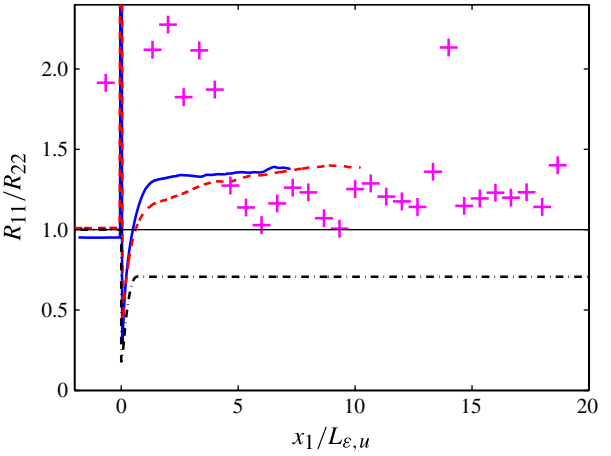

FIGURE 10. (Colour online) Evolution of the turbulence anisotropy R_{11}/R_{22} at $(M, M_t) \approx (3.50, 0.16)$ and $Re_\lambda = 40$ (solid) and 74 (dashed), compared to results from linear interaction analysis (dash-dotted) taken from Sinha, Mahesh & Candler (2003), and experiments (symbols) by Barre *et al.* (1996) using LDV.

does not change. The latter implies that the post-shock adjustment process occurs over turbulence length scales rather than acoustic ones.

Figure 9 also shows a zoom around the shock for a single case. The large peak around the shock is solely due to unsteady shock movement, and not turbulence. This can be illustrated by using the simple model for the instantaneous shock-normal velocity:

$$u_1(x, \xi) = \begin{cases} u_{1,u}, & x < x_s(\xi), \\ u_{1,d}, & x > x_s(\xi), \end{cases} \tag{3.1}$$

where x_s is the instantaneous shock position and ξ is a random variable. In other words, the velocity field is assumed to be non-turbulent with a randomly varying shock position. It is then easy to show that this model implies (regardless of the random number distribution) the variance $\overline{u_1' u_1'} = (u_{1,u} - \overline{u}_1)(\overline{u}_1 - u_{1,d})$, which is shown in the figure by the dashed line. The agreement at the shock shows that the peak in R_{11} in that location is almost entirely due to the unsteady shock movement. As a side point, we note that the region of unsteady shock movement (the grey strip in the figure) is defined here as the region of mean fluid compression.

We next compare the computed Reynolds stresses to the experimental data of Barre *et al.* (1996), who generated approximately isotropic turbulence using a multi-nozzle in a supersonic wind tunnel. The experimental conditions were different from the ones in the DNS: specifically $M = 3$, $M_t \approx 0.01$ and a turbulent Reynolds number based on the dissipation length scale of order 30 (estimated from the information in the paper).

The evolution of the turbulence anisotropy R_{11}/R_{22} is shown in figure 10 and is considered first. The two DNS cases at different Reynolds numbers show a fairly constant level of anisotropy behind the shock, with no evidence of a return to isotropy within the (admittedly short) domain. The experimental data similarly show an essentially constant level of post-shock anisotropy, at a slightly lower level: about 1.2 compared to 1.3 in the DNS.

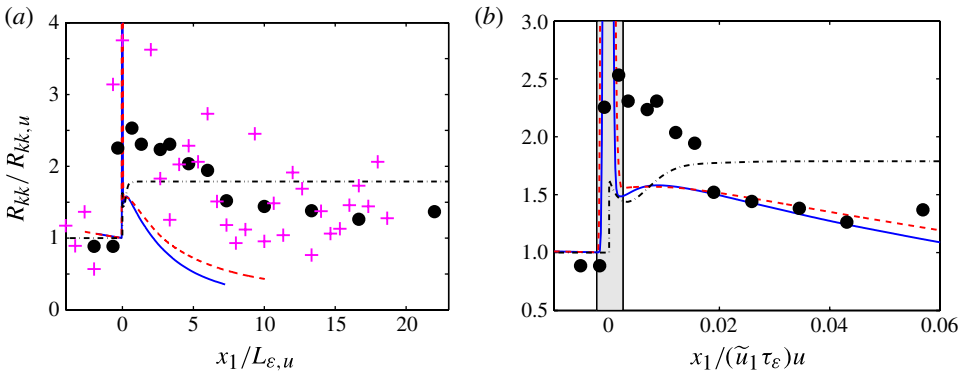

FIGURE 11. (Colour online) Evolution of the turbulence kinetic energy $R_{kk}/2$ at $(M, M_t) \approx (3.50, 0.16)$ and $Re_\lambda = 40$ (solid) and 74 (dashed), compared to results from linear interaction analysis (dash-dotted) taken from Sinha *et al.* (2003), and experiments by Barre *et al.* (1996), where the plus symbols show the raw LDV measurements and the solid circles show the results of combining hot-wire data of R_{11} with LDV data of R_{11}/R_{22}. The shock-normal coordinate x_1 is normalized by (*a*) the dissipation length scale and (*b*) the convected time scale, in the respective panels. The grey strip in panel (*b*) shows the region of unsteady shock movement.

We next consider the evolution of the turbulence kinetic energy in figure 11, using two different normalizations of the shock-normal coordinate. First, it is clear that there is a considerable spread in the LDV data. The hot-wire data are much cleaner, but collected only for the R_{11} component. By using the experimental result for the anisotropy R_{11}/R_{22} discussed above, the hot-wire data can be used to estimate the trace of the Reynolds stress; this is shown in solid symbols in the figure. When the shock-normal coordinate is normalized using a characteristic length scale of the turbulence (the dissipation length scale), there is considerable disagreement. This disagreement, however, is entirely due to the differing conditions between the DNS and the experiment, and, specifically, how the shock-normal coordinate is normalized. After the post-shock adjustment, the main physical process is simply decay of the turbulence. This implies that the relevant length scale is a convected turbulence decay time scale, i.e. $\widetilde{u}_1\tau_\varepsilon = \widetilde{u}_1 L_\varepsilon/\sqrt{R_{kk}/2}$; this normalization is used in figure 11(*b*). The agreement for $x_1 \gtrsim 0.02\,\widetilde{u}_{1,u}\tau_{\varepsilon,u}$ between the DNS and the experiment is quite remarkable.

3.2. *Reynolds stresses: budgets*

The Reynolds stress equation (cf. Wilcox 2000) can be simplified considerably for the present case of canonical shock–turbulence interaction. Moreover, away from the shock, several terms are negligible. Thus to a good approximation the Reynolds stress equations can be written as

$$\partial_1(\overline{\rho}\,\widetilde{u}_1 R_{kk}) \approx -2\overline{\sigma_{kj}\partial_j u_k''} + 2\overline{p'\partial_k u_k''} - 2\partial_1\overline{p'u_1''}, \tag{3.2a}$$

$$\partial_1(\overline{\rho}\,\widetilde{u}_1 R_{11}) \approx -2\overline{\sigma_{1j}\partial_j u_1''} + 2\overline{p'\partial_1 u_1''} - 2\partial_1\overline{p'u_1''}, \tag{3.2b}$$

$$\partial_1(\overline{\rho}\,\widetilde{u}_1 R_{22}) \approx -2\overline{\sigma_{2j}\partial_j u_2''} + 2\overline{p'\partial_2 u_2''}. \tag{3.2c}$$

The terms on the right are, in order, viscous dissipation, pressure–strain correlation and pressure–velocity transport. Note that $\overline{\rho}\,\widetilde{u}_1$ is constant (by virtue of mass conservation),

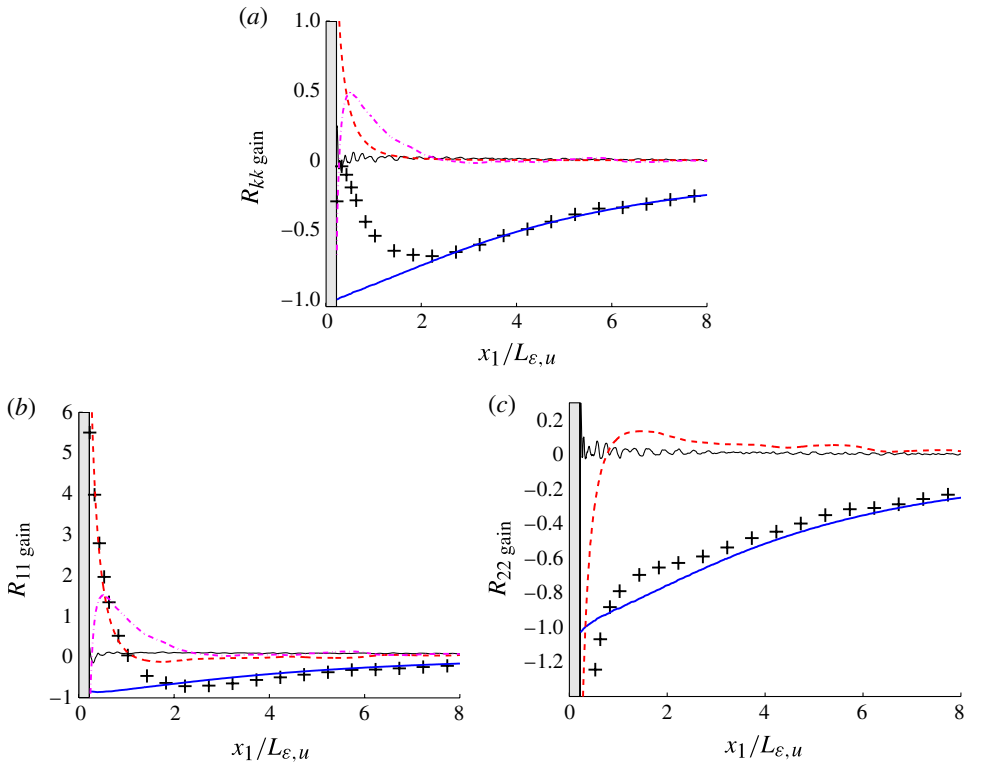

FIGURE 12. (Colour online) Reynolds stress budget for $(M, M_t) = (1.50, 0.14)$ and $Re_\lambda = 73$. Viscous dissipation (thick solid), pressure–strain (dashed), pressure–velocity (dash-dotted), the sum of these three terms (symbols), and the sum of these three terms plus the mean convection (thin solid line around zero). All terms are scaled by the corresponding value of $\overline{\rho}\varepsilon_{ij}$ taken immediately behind the shock. The grey strip shows the region of unsteady shock movement.

and hence equations (3.2) represent the rate of change of the Reynolds stresses. The budget for one representative case is shown in figure 12.

To establish the quality of the budgets computed from the DNS data, the thin solid lines in figure 12 show the sum of all terms in (3.2) (with the mean convection moved to the right-hand side). The deviation from zero is the error in (3.2), due to both neglected terms and finite averaging. The error is an order of magnitude smaller than the results.

The viscous dissipation is dominant for $x_1/L_{\varepsilon,u} \gtrsim 2$; in fact, it is the only non-negligible term for the evolution of the turbulence kinetic energy. The pressure–velocity term is significant in the post-shock adjustment region, where it contributes to the growth of R_{11} and R_{kk}. The pressure–strain term is very large behind the shock but quickly decreases in magnitude. For $x_1/L_{\varepsilon,u} \gtrsim 1$, it becomes slightly positive for the transverse stresses and equally negative for the shock-normal stress, and thus contributes to a (very slow) return to isotropy. The effect on the kinetic energy (a pressure-dilatation correlation) is negligible. The shape and characteristic length scale of the pressure–strain term is quite constant for different M, M_t and Re_λ.

The most interesting use of the budget terms is to artificially remove the viscous dissipation from the resulting profiles. The integrated right-hand side of the budget

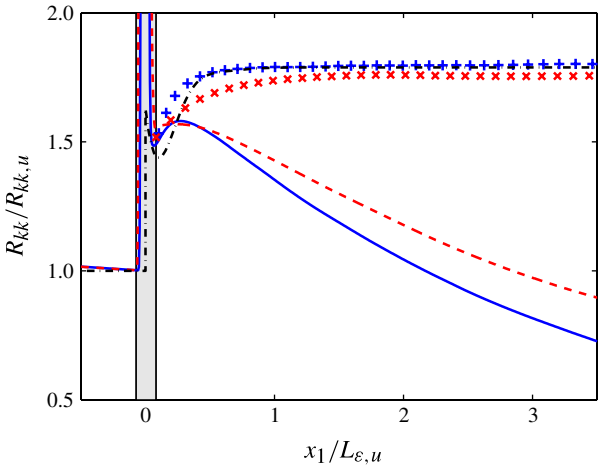

FIGURE 13. (Colour online) Using the integrated dissipation term to extrapolate to infinite Reynolds number at $(M, M_t) \approx (3.50, 0.16)$. Raw DNS results (decaying profiles) at Re_λ of 40 (solid) and 74 (dashed); DNS results with artificially removed viscous dissipation (equation (3.4); see text for details) at Re_λ of 40 (plus) and 74 (cross); compared to linear theory (dash-dotted). The grey strip shows the region of unsteady shock movement.

equations (3.2) over an interval equals the change in Reynolds stress over that same interval. Thus (where $R_{\alpha\alpha}$ denotes either R_{11}, R_{22} or R_{kk})

$$R_{\alpha\alpha}(x_1) = R_{\alpha\alpha}(x_{1,0}) + \frac{1}{\overline{\rho}\,\widetilde{u}_1}\int_{x_{1,0}}^{x_1} ([\text{Diss.}] + [\text{Rem.}])\,\mathrm{d}x_1', \tag{3.3}$$

where the mean mass flux is constant and hence can be taken outside the integral, and where [Diss.] and [Rem.] represent the viscous dissipation and all remaining terms, respectively. Provided that $x_{1,0}$ is taken from behind the shock, this reconstructs the profile to within very small numerical integration errors; across the shock, the numerical integration errors in (3.3) are substantial.

One can therefore define

$$R^*_{\alpha\alpha} = R_{\alpha\alpha}(x_{1,0}) + \frac{1}{\overline{\rho}\,\widetilde{u}_1}\int_{x_{1,0}}^{x_1} [\text{Rem.}]\,\mathrm{d}x_1' = R_{\alpha\alpha} - \frac{1}{\overline{\rho}\,\widetilde{u}_1}\int_{x_{1,0}}^{x_1} [\text{Diss.}]\,\mathrm{d}x_1' \tag{3.4}$$

as the Reynolds stress with the effect of viscous dissipation removed: i.e. an artificial extrapolation to infinite Reynolds number. This type of profile is shown in figure 13 for two cases, where it is clear that the modified profiles agree quite well with the result of linear theory.

3.3. *Reynolds stresses: change due to the shock interaction*

The size of the post-shock adjustment region is about L_ε, i.e. about one characteristic large eddy size. In most practical applications, this is small relative to the main features of the flow, and hence the most important result of a shock–turbulence interaction is the effect on the post-shock turbulence after this adjustment, i.e. in the far field. Therefore, the modification to turbulence by a shock should be defined using the far-field values of R_{ij}.

The turbulence anisotropy R_{11}/R_{22} is approximately constant in the post-shock region, and thus its far-field value is easily computed. For the TKE $R_{kk}/2$, however, the

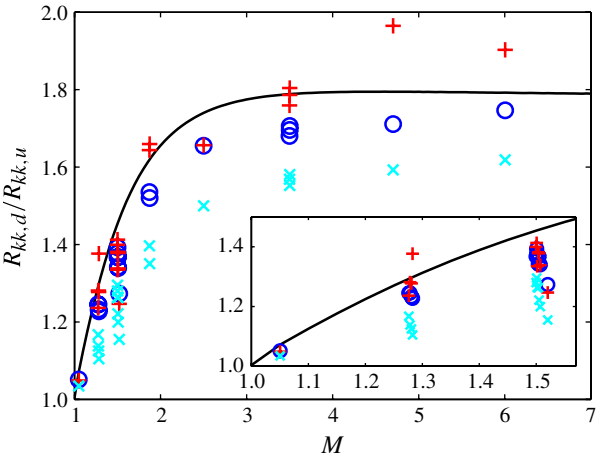

FIGURE 14. (Colour online) Amplification of the TKE across the shock versus Mach number, using different definitions of the post-shock state. DNS with spatial extrapolation to the mean shock position (circle, the technique used in figure 15), DNS with artificially removed viscous dissipation (plus, see text for details), and linear theory (solid, taken from Sinha *et al.* (2003)). Also shown are the values from DNS computed at the post-shock peak (cross).

significant viscous decay in the DNS results makes it difficult to define unambiguously the amplification induced by the shock. Some studies in the literature (e.g. Donzis 2012*a*) define the amplification through the value at the post-shock peak in R_{kk}. While well defined, this introduces an effect of the Reynolds number, as a result of the viscous decay occurring up to the post-shock peak. An alternative is to spatially extrapolate the R_{kk} profile back to the mean shock position (cf. Larsson & Lele 2009). This is less well defined, but potentially avoids the Reynolds-number effect.

These different definitions are compared in figure 14. Unsurprisingly, the spatial extrapolation leads to larger computed amplification factors compared to using the post-shock peak. There are multiple cases at different Re_λ and M_t at several values of the mean Mach number; while there is some spread among these cases using both definitions, the spread is arguably smaller when using the spatial extrapolation.

The modified R^*_{kk} defined in (3.4), where the effect of viscous dissipation has been artificially removed, can be used to define yet another amplification factor across the shock. Since this artificial quantity is constant in the far field, the value there can be directly used to compute the amplification of R_{kk}; this is also shown in figure 14. The resulting amplification factors are similar to or slightly larger than those obtained with spatial extrapolation.

The predicted amplification from linear analysis is between the values estimated using spatial extrapolation and the artificial profiles (which can be viewed as extrapolations to infinite Reynolds number). Overall, these results suggest rather strongly that the linear theory of Ribner (1954) accurately describes and predicts the amplification of TKE.

The amplification factors are shown again in figure 15, using the results of the spatial extrapolation only. In this figure the symbols denote different values of Re_λ and M_t. Close inspection reveals a very small dependence on the Reynolds number, but a slightly larger dependence on the turbulent Mach number (or, similarly, the turbulence intensity). Specifically, the amplification factors consistently decrease for more intense

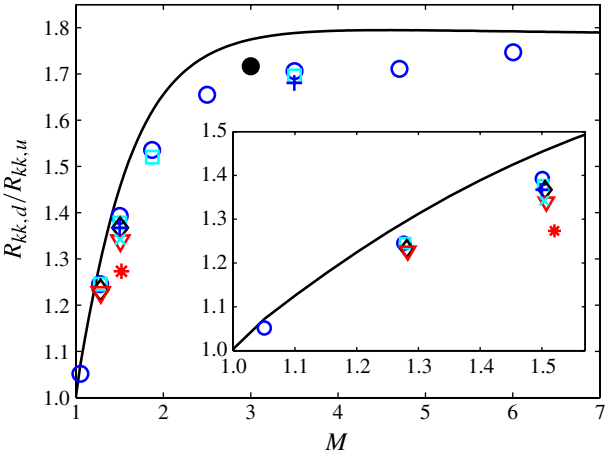

FIGURE 15. (Colour online) Amplification of the TKE across the shock versus Mach number, where the post-shock R_{kk} is defined through spatial extrapolation to the mean shock position. At each Mach number, the cases are shown with different symbols in order of increasing M_t. At $Re_\lambda \approx 40$ the symbols are, in order: circle, square, diamond, and triangle. At $Re_\lambda \approx 70$ the symbols are, in order: plus, cross, and star. Also shown for comparison are results from linear interaction analysis (solid), taken from Sinha *et al.* (2003), and experiments (solid circle) by Barre *et al.* (1996) using hot-wire anemometry for R_{11} combined with LDV measurements of R_{11}/R_{22}.

turbulence. This is consistent with the decrease in the mean compression at higher M_t, as discussed earlier.

The amplification computed from the experiment by Barre *et al.* (1996) (which was also extrapolated back to the shock position) is also included in the figure. There is a close agreement between the experiment, the linear analysis and the DNS results.

The turbulence anisotropy in the far field is shown in figure 16. Given the essentially constant values of this quantity in the post-shock region, no extrapolation is necessary for this quantity. There is a qualitative disagreement with Ribner's linear analysis for $M \gtrsim 1.3$, where the linear theory predicts a decreasing anisotropy (with the Mach number) and, in fact, that the transverse Reynolds stress R_{22} should be larger than the shock-normal R_{11} for $M > 1.9$. Both the DNS and the experiment give anisotropies of type $R_{11} > R_{22}$ for all Mach numbers. This strongly suggests that the generation of turbulence anisotropy during the interaction with a shock is a nonlinear process, driven by the significant pressure–strain and pressure–velocity terms in the immediate post-shock region.

3.4. *Vorticity variances*

Sample profiles of vorticity variances through the shock are shown in figure 17. All cases give results that are qualitatively similar. The transverse vorticity is amplified instantaneously during the shock interaction, whereas the shock-normal component is initially unaffected by the interaction. A short distance behind the shock, however, the vorticity components return to isotropy, thus suggesting that the small scales return to isotropy as well. The distance over which this occurs clearly decreases with Reynolds number. In fact, the proper length scale to describe this phenomenon is the convected Kolmogorov time scale. This is shown in figure 18, where the anisotropy is defined to account for the different amplification ratios of the transverse component at

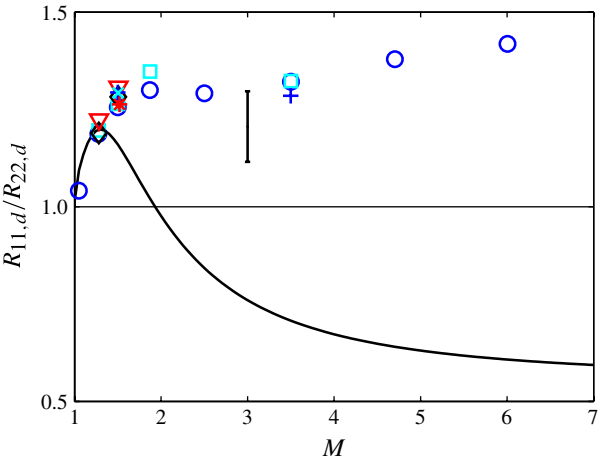

FIGURE 16. (Colour online) Mach number dependence of the post-shock turbulence anisotropy in the far field. At each Mach number, the cases are shown with different symbols in order of increasing M_t. At $Re_\lambda \approx 40$ the symbols are, in order: circle, square, diamond, and triangle. At $Re_\lambda \approx 70$ the symbols are, in order: plus, cross, and star. Also shown for comparison are results from linear interaction analysis (solid), taken from Sinha *et al.* (2003), and experiments by Barre *et al.* (1996) using LDV (error bar showing the experimental root-mean-square variation in the far field).

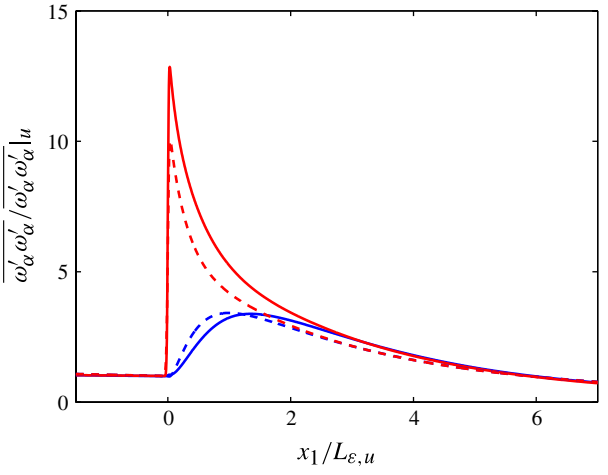

FIGURE 17. (Colour online) Evolution of vorticity variances at $(M, M_t) = (3.50, 0.16)$ and Re_λ of 40 (solid) and 74 (dashed). Shock-normal ($\overline{\omega'_1\omega'_1}$, lower curves) and transverse ($\overline{\omega'_2\omega'_2}$, upper curves) components.

different Mach numbers. There is a high degree of collapse in the return to isotropy of the vorticity, which occurs over a distance of about 10 convected Kolmogorov time scales. At high Reynolds numbers, this distance would become very small, perhaps too small to detect in experiments. The anisotropic amplification of vorticity across the shock is, therefore, of little practical importance. For example, in Reynolds averaged Navier–Stokes (RANS) modelling of the dissipation rate (or surrogates thereof), the objective must be to predict the change from pre-shock to after the post-shock

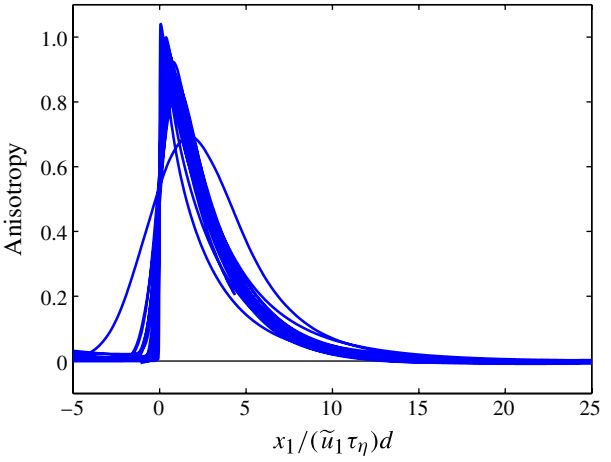

FIGURE 18. (Colour online) Anisotropy of vorticity variances for all cases, where the anisotropy is defined as $(\overline{\omega_2'\omega_2'} - \overline{\omega_1'\omega_1'})/(\overline{\omega_2'\omega_2'}|_d - \overline{\omega_2'\omega_2'}|_u)$. The outlier corresponds to $(M, M_t) = (1.52, 0.38)$ and $Re_\lambda = 72$.

adjustment. Similarly, since large-eddy simulation (LES) is aimed at high Reynolds numbers with filter widths far exceeding the Kolmogorov scale, there is no reason to expect that small-scale anisotropy behind the shock could be captured.

4. Interaction regimes

At Reynolds numbers of practical interest, the shock is an inviscid phenomenon and essentially a discontinuity. The incoming turbulence perturbs the shock beyond its nominally planar shape. To illustrate the wide difference in instantaneous shock interactions that occur for intense turbulence, consider the shock and three pathlines through the shock shown in figure 19. The instantaneous shock is highly corrugated and shows a large range of instantaneous density jumps across it.

To quantify these departures from the mean, we define the instantaneous shock location $x_s(x_2, x_3, t)$ as the position along the shock-normal direction (x_1) where the minimum dilatation occurs (i.e. maximum fluid compression). Given this, the instantaneous density jump across the shock $\Delta\rho_s(x_2, x_3, t)$ is then defined as the maximum difference in density between the two grid points upstream and downstream of $x_s(x_2, x_3, t)$. While clearly numerical in nature, this definition is consistent with the known nature of the WENO shock-capturing scheme to capture a shock in two or three grid points. We also note that the Kolmogorov length scale downstream of the shock is between 1.5 and 3 times the shock-normal grid spacing for all cases; thus our definition of the shock jump is effectively to compare the density values about one Kolmogorov length upstream and downstream of the shock, respectively. By including two grid points before and after the shock location, the computed $\Delta\rho_s$ is a very reasonable approximation to the instantaneous shock jump even in a highly turbulent flow field.

With these definitions, the excursions of the shock in figure 19 are $-0.4 \lesssim x_s/L_\varepsilon \lesssim 0.3$, with $\Delta\rho_s$ going from virtually zero to more than three times its mean value. The regions of the shock with virtually zero compression were termed 'shock holes' in Larsson & Lele (2009), and the presence or absence of instantaneous shock holes was

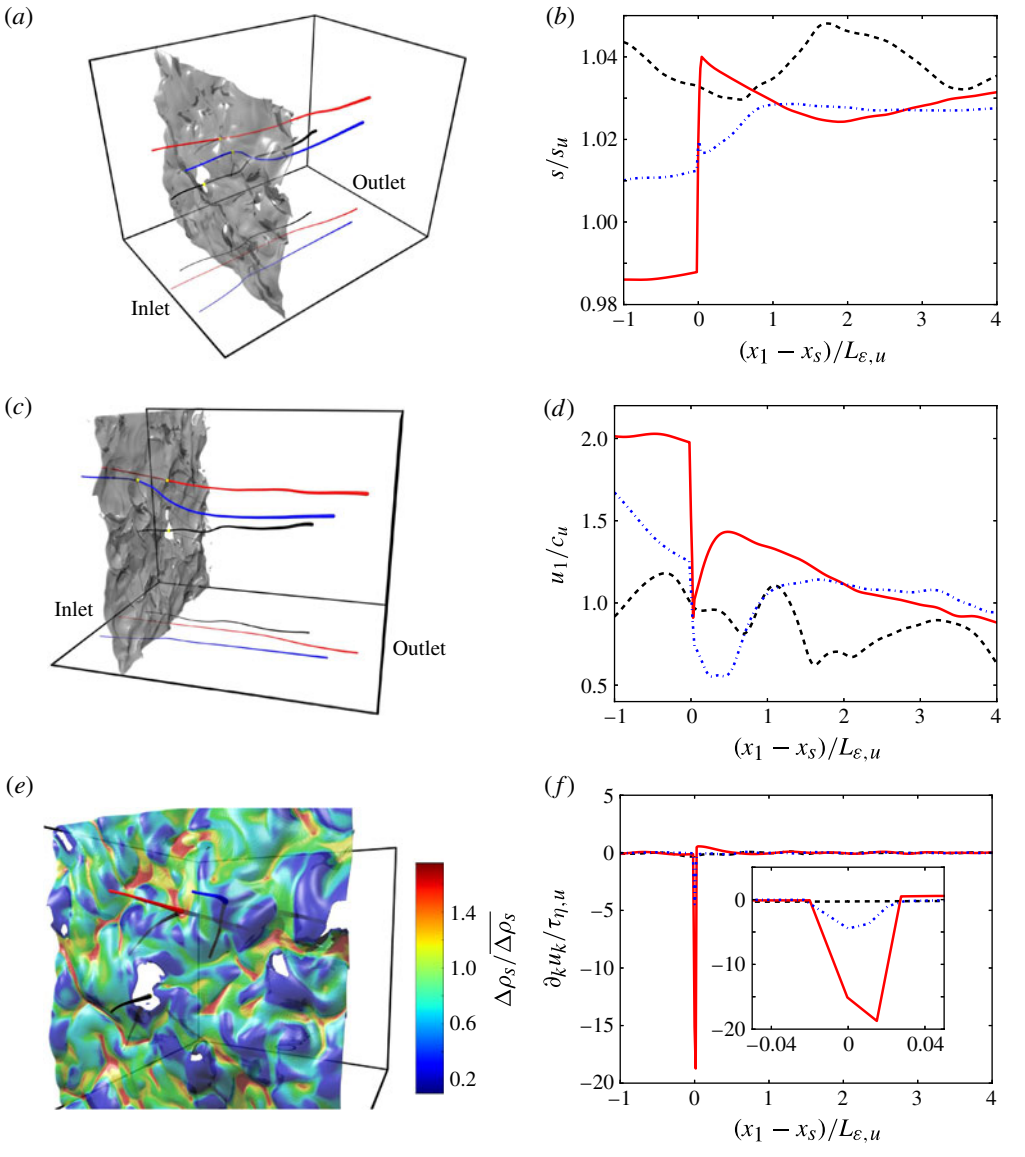

FIGURE 19. Instantaneous pathlines of three fluid particles at $(M, M_t) = (1.51, 0.37)$ and $Re_\lambda = 39$ that crossed the shock at the same time, in regions of very high compression (solid), relatively low compression (dash-dotted) and virtually zero compression (a 'shock hole', dashed line). (*a*,*c*) 3D views of the pathlines together with an isosurface of negative dilatation visualizing the shock (grey surface) at the time when the particles traverse it (marked by a pale/yellow dot for each particle). The projections of the pathlines on the bottom plane of the domain are included for clarity. (*e*) A zoomed view of the particle trajectories at the instant when they crossed the shock, with the shock shaded/coloured by the local density jump across it, normalized with the average density jump. (*b*,*d*,*f*) Traces of entropy, shock-normal velocity and dilatation along the three pathlines, plotted as functions of the shock-normal coordinate relative to the shock position at the time the particle crossed the shock.

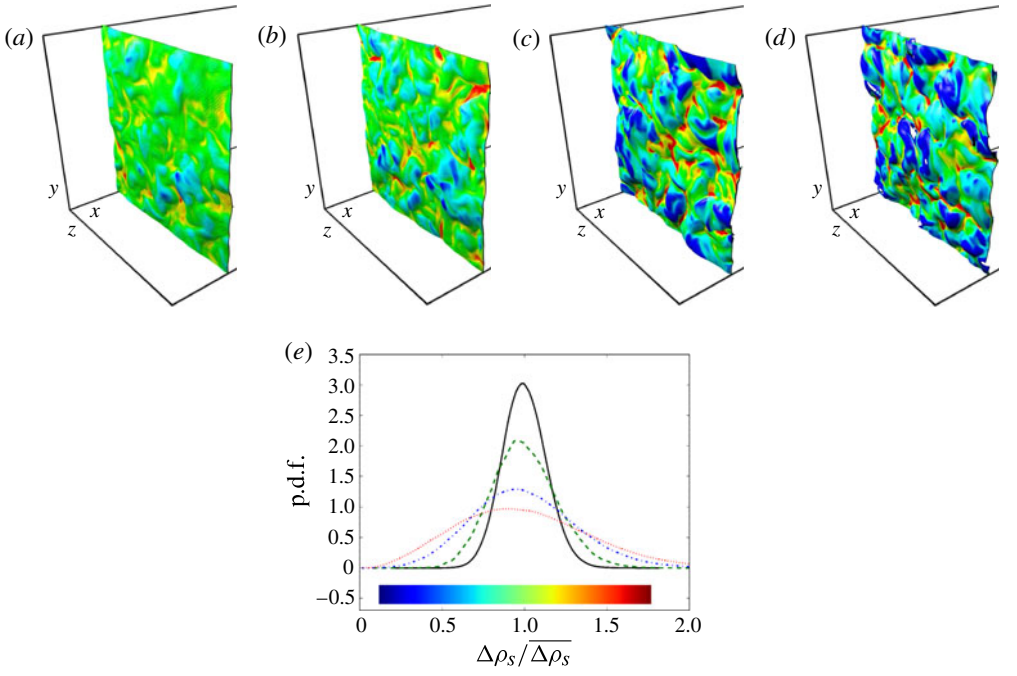

FIGURE 20. Instantaneous shock strength and shape for increasing M_t at fixed $M \approx 1.50$ and $Re_\lambda \approx 40$. (*a–d*) Instantaneous shock educed through isocontour of negative dilatation coloured by the density jump, $\Delta\rho_s$, for $M_t = 0.15,\ 0.22,\ 0.31,\ 0.37$ (from left to right). (*e*) The p.d.f. of the normalized density jump for M_t of 0.15 (solid), 0.22 (dashed), 0.31 (dash-dotted) and 0.37 (dotted).

used to classify the shock–turbulence interaction into the 'broken shock' (with shock holes) or 'wrinkled shock' (without) regimes, respectively.

Figure 19 also shows the traces of several quantities along three pathlines that traversed the shock at the same time. At the time of shock crossing, the pathlines crossed the shock in regions of very high, rather low and virtually zero compression, respectively. The fluid particle that passed through a shock hole has completely smooth profiles of all quantities, with no discernible interaction with the shock at all. Note that the velocity of this particle was only slightly supersonic as it approached the shock, with a smooth decrease through the sonic point. This statement comes with two caveats: first, the averaged speed of sound is used in the figure, and, secondly, the velocity is in the frame of the mean, not instantaneous, shock. Nevertheless, the fact that the shock hole is associated with near-sonic flow approaching the shock will be used below in defining a criterion for which regime the interaction is in.

While the numerical method is not the focus of this paper, we note that the solution-adaptive method reverts to the central difference scheme in the shock holes. For the case shown in figure 19, the WENO scheme is used at points where the rate of dilatation $\partial_k u_k \lesssim -1$ (on average); as can be seen in the figure, the trace through the shock hole never comes close to this limit.

4.1. *Instantaneous shock strength*

The effect of increasingly intense turbulence on the shock is illustrated in figure 20. The four cases shown have M_t from 0.16 to 0.37, or turbulence intensities from 6 to

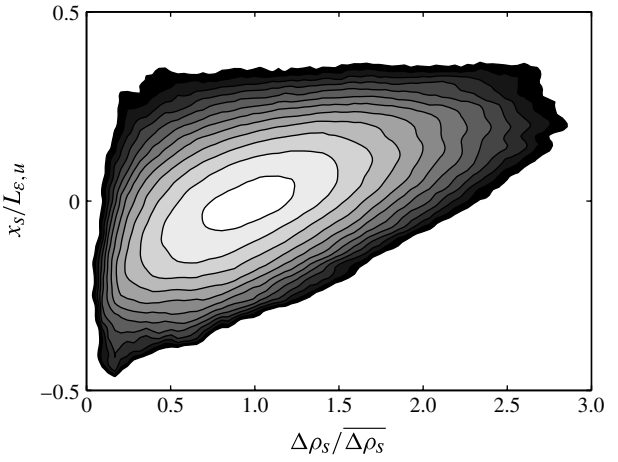

FIGURE 21. Joint p.d.f. of the instantaneous density jump across the shock $\Delta\rho_s$ and the instantaneous shock position x_s at $(M, M_t) = (1.51, 0.37)$ and $Re_\lambda = 39$. Contours spaced logarithmically from the peak (light) down to three decades lower (dark).

14 %. The increasing corrugation of the shock is clear, as is the increasing prevalence of very large or small local fluid compressions. This is further illustrated in the probability density function (p.d.f.) of $\Delta\rho_s$, which broadens substantially for more intense turbulence.

Figure 21 shows the joint p.d.f. of the density jump and the shock location. Strong shock events are correlated with a pushed-back shock, and vice versa; this is consistent with observations by Lee *et al.* (1993). This makes sense in two ways. First, the local shock velocity increases with shock strength, thus implying that displaced shock segments return towards the mean position. If this were not the case, the configuration would be unstable. Secondly, by geometrical reasoning, a pushed-back shock would have a concave curvature, which by focusing of the post-shock flow would imply a higher post-shock density, i.e. a stronger shock.

The p.d.f.s of the density jump are very insensitive to the Reynolds number, as shown in figure 22. This suggests that the presence of shock holes is not an effect of low Reynolds number. Specifically, one might have expected that larger viscous forces would more easily overcome the inviscid shock compression. While undoubtedly true, the collapse of the p.d.f.s in the figure suggests that this would happen only for Reynolds numbers significantly lower than those considered here.

4.2. *Grid convergence of shock-jump p.d.f.s*

The present study is a DNS in the extended sense of fully resolving all scales of turbulence but capturing the shock discontinuity numerically. A discussion on the accuracy and realism of this approach was given in § 2, including theoretical arguments and grid convergence verification that strongly suggest that the post-shock statistics are unaffected by the numerical shock-capturing technique. Let us take this question one step further. One key finding in the study of Larsson & Lele (2009) was the presence of smooth instantaneous profiles through the shock; further examples of such smooth profiles were shown above as well. It is then important to verify that these instantaneously smooth interactions are physical, and not artefacts of the numerical shock-capturing scheme.

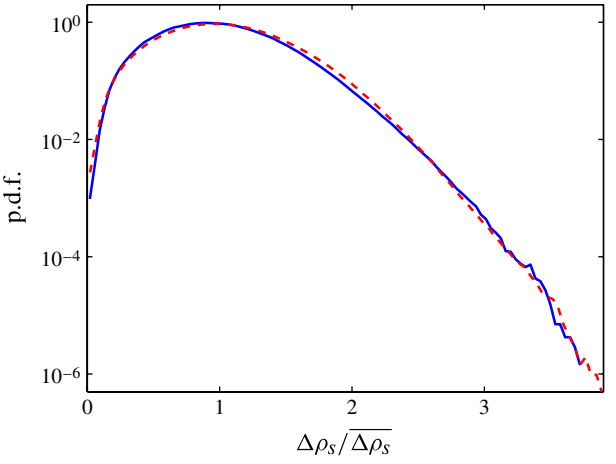

FIGURE 22. (Colour online) The p.d.f. of the instantaneous density jump across the shock $\Delta\rho_s$ at $(M, M_t) \approx (1.50, 0.38)$ and Re_λ of 39 (solid) and 72 (dashed).

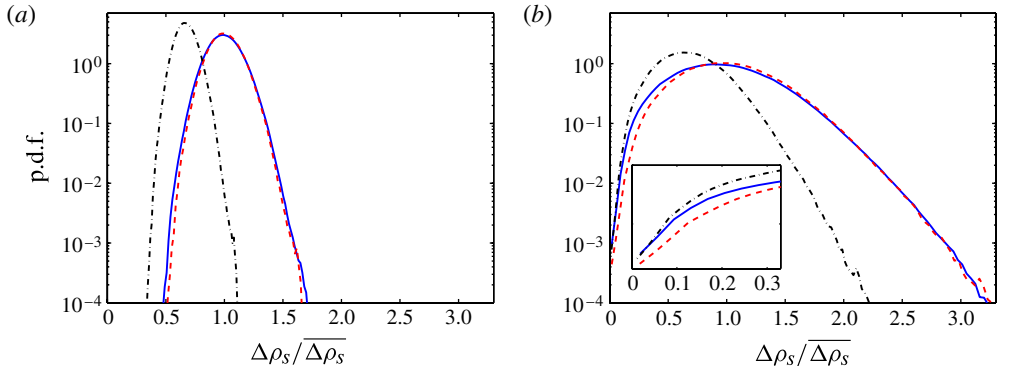

FIGURE 23. (Colour online) The p.d.f. of the instantaneous density jump across the shock $\Delta\rho_s$ at $M \approx 1.50$ and $Re_\lambda \approx 40$ computed on the finest 1040×384^2 grid (solid): (*a*) $M_t = 0.15$; (*b*) $M_t = 0.37$, with inset showing a zoom around small density jumps. Also shown for comparison is the p.d.f. computed on a coarser 694×256^2 grid in two different scalings: raw (dashed) and with $\Delta\rho_s$ scaled by the ratio of fine to coarse grid spacing (dash-dotted).

Consider the quantity $\Delta\rho_s$ and how it depends on the grid resolution h. For discontinuous solutions, the jump is, by definition, unaffected by the grid spacing. For smooth solutions, the jump as defined here (the density difference within a local numerical stencil) must scale as $\partial_1\rho\, h$, i.e. proportional to h. Given the chaotic nature of the flow, it is impossible to perform a grid refinement study on these instantaneous events. However, the events do appear in the p.d.f. of $\Delta\rho_s$.

Figure 23 shows this p.d.f. computed on the finest and next coarsest grids for two cases. At low M_t these two p.d.f.s agree very well with each other across the full range of $\Delta\rho_s$, but at high M_t there is a disagreement at low density jumps. If we hypothesize that the events in the region of disagreement are smooth interactions, then the p.d.f.s should instead collapse when scaled by the grid spacings; this is also shown in the figure, and collapse is seen for $\Delta\rho_s \lesssim 0.1\overline{\Delta\rho_s}$ at the highest M_t. This offers statistical

evidence that there exists instantaneously smooth profiles through the shock, provided the turbulence is sufficiently intense. Specifically, the convergence of the p.d.f.s under different scalings shows that the existence of the smooth profiles is not an artefact of the numerical scheme.

The fact that the p.d.f.s from two different grids collapse in 'smooth' scaling for $\Delta\rho_s \lesssim 0.1\overline{\Delta\rho_s}$ implies that the majority of points on the shock that experience such instantaneous jumps have smooth compressions through the 'shock'; they are 'shock holes'. From the p.d.f., this range of shock jumps occurs for only about 0.05 % of the points on the shock surface. The different p.d.f.s collapse in 'discontinuity scaling' for $\Delta\rho_s \gtrsim 0.6\overline{\Delta\rho_s}$, which corresponds to about 90 % of the points on the shock surface. The p.d.f.s in the intermediate interval collapse in neither scaling, implying that a mixture of smooth and discontinuous events occur for density jumps in this interval. Thus the fraction of the shock that experiences smooth compressions is certainly larger than 0.05 % but less than 10 %; if we pick the point where the fine-grid p.d.f. is halfway between the differently scaled coarse-grid p.d.f.s, we get that about 1 % of the shock surface is locally (in space and time) occupied by shock holes.

4.3. *Criterion for the 'wrinkled' and 'broken' shock regimes*

The existence of different regimes in the shock–turbulence interaction process is clear. The regimes were dubbed the 'wrinkled' and 'broken' shock regimes in Larsson & Lele (2009), to describe whether the shock retains its structure or not. Lee *et al.* (1993) argued that the interaction should be in the broken regime when the pressure fluctuations induced by the turbulence in the upstream flow are large compared to the pressure jump across the shock; this then led to a parameter $M_t^2/(M^2-1)$.

In the present work a different argument is used, leading to the different controlling parameter $M_t/(M-1)$. This is similar (except for the Reynolds-number dependence) to the parameter $K = M_t/[\sqrt{Re_\lambda}(M-1)]$ arrived at by Donzis (2012*a*) using similarity arguments about the instantaneous shock thickness. In follow-up work, as part of a deeper theoretical analysis of the shock–turbulence interaction problem, Donzis (2012*b*) then used arguments very similar to those used here (but developed independently) to arrive also at $M_t/(M-1)$ as the controlling parameter for the interaction regimes.

Consider the instantaneous traces along pathlines in figure 19. Among these three pathlines, the strongest shock compression is associated with the highest approach velocity and vice versa. In fact, the velocity leading up to the shock hole smoothly reaches sonic speed before the 'shock', suggesting that this was caused solely by the upstream turbulence. Several caveats are in order (mentioned above, but worth repeating): the averaged speed of sound was used in the figure, the velocity is in the frame and direction of the averaged shock, and we only showed three events here. Despite these caveats, it is still tempting to hypothesize that shock holes are created whenever there is a finite (and likely sufficiently large) probability of subsonic flow upstream of the shock. Let us assume that the incoming shock-normal velocity u_1 can be described by a p.d.f. $P(u) = Q(s)/u'_{rms}$, where $s = (u-\overline{u})/u'_{rms}$ and $Q(s)$ is assumed universal for all turbulence M_t and Re_λ. The probability of subsonic flow (in the frame of the mean shock position) is then

$$\beta = \int_{-\infty}^{c} P(u)\,\mathrm{d}u = \int_{-\infty}^{(c-\overline{u})/u'_{rms}} Q(s)\,\mathrm{d}s. \tag{4.1}$$

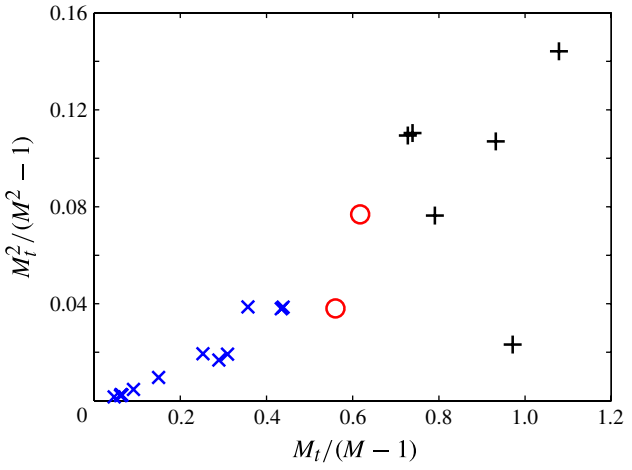

FIGURE 24. (Colour online) Regime diagram comparing the parameter $M_t/(M-1)$ with the one proposed by Lee *et al.* (1993): cases in the wrinkled shock regime (cross), broken shock regime (plus) and two borderline cases (circle).

If Q is universal, then β is an increasing function of $M_t/(M-1)$. Therefore, the probability of subsonic flow will be larger than some threshold whenever $M_t/(M-1)$ is larger than some critical value.

The arguments about how the p.d.f. of the density shock jump should scale under grid refinement can then be used to classify every case. Cases where the unscaled p.d.f.s on two grids agree everywhere are in the wrinkled shock regime, whereas cases where the scaled p.d.f.s on two grids agree at least somewhere are in the broken shock regime. Two cases were found to satisfy neither of these criteria: for small density jumps, neither scaling of the p.d.f. collapses well. These cases are classified as borderline here.

A scatter plot is shown in figure 24. The present parameter $M_t/(M-1)$ clearly demarcates cases in the different regions, with $M_t \gtrsim 0.6(M-1)$ being a reasonable criterion for the broken shock regime. The parameter proposed by Lee *et al.* (1993) does a reasonable job, but is erroneous for the point in the lower right corner; this point corresponds to $(M, M_t) = (1.05, 0.05)$, a case which was run solely to demonstrate this point.

5. Summary

A sequence of DNS of isotropic turbulence interacting with a normal shock wave is presented. The DNS data spans mean Mach numbers from 1.05 to 6, turbulent Mach numbers from 0.05 to 0.38, and Taylor-scale Reynolds numbers from 40 to 70. The DNS results are verified by assessing the sensitivity of the results to the grid resolution and the computational box size, and validated by comparing the TKE and Reynolds stress anisotropy with the experimental data of Barre *et al.* (1996).

The mean density jumps across all conditions are found to be about a factor $0.95\,(M_t/M)^2$ lower than the Rankine–Hugoniot results for inviscid flow; the correction factor for the mean pressure jumps is a factor $\gamma = c_p/c_v$ higher. This is in qualitative but not quantitative agreement with the theoretical analysis of Lele (1992).

The arguably most important effect of a shock–turbulence interaction is the amplification of TKE. Given the difficulty of accurately measuring close to the

shock in experiments, and the rapid viscous decay in simulations, there are different definitions of the amplification factor in the literature. In this study three different methods are used to define the amplification of TKE: the post-shock peak TKE, the post-shock TKE extrapolated back to the mean shock position, and a 'modified' far-field TKE computed from the budget equation by ignoring the dissipation term. There are differences among the amplification factors computed using these three methods, but the latter two methods produce results that are relatively close to each other. This relative closeness in the results, despite the rather different means of removing the Reynolds-number effect, can be taken as some form of consistency check on the amplification factors computed using these two methods (extrapolation and 'modified' far-field TKE). Moreover, these amplification factors agree quite well with those predicted by the linear theory of Ribner (1954). Therefore, at least this one key aspect of the interaction (between two distinctly nonlinear phenomena, turbulence and a shock wave) can be accurately represented using linear theory.

In contrast, the linear theory predicts highly anisotropic amplification of vorticity (zero amplification of streamwise vorticity). Early simulations by Lee *et al.* (1993, 1997) essentially verified this prediction. The present study, however, suggests that this prediction, while true, has little practical importance: the post-shock vorticity is found to reach isotropy about 10 convected Kolmogorov time scales behind the shock, for all conditions computed here. Since vorticity is a small-scale phenomenon, this makes perfect sense. In realistic applications, with high Reynolds numbers and small Kolmogorov scales (relative to other scales of interest), the post-shock vorticity (and small scales in general) can be considered isotropic for most practical purposes.

The possibility of large excursions around the mean of the local, instantaneous shock strength has previously been reported experimentally (by Hesselink & Sturtevant (1988), at $M \leqslant 1.1$ in a random medium) and computationally (first by Lee *et al.* (1993), at $M = 1.05$; later by Larsson & Lele (2009), at M up to 1.5). In the present study this is confirmed through visualization of the distorted shocks at different turbulence intensities. The probability density function (p.d.f.) of the local shock strength is shown to be very insensitive to the Reynolds number, implying that these effects are due purely to inviscid interactions between the incoming turbulence and the shock wave. Furthermore, comparison of the p.d.f.s computed at different grid resolutions shows that the presence of 'shock holes', i.e. events where the shock locally disappears, is not an artefact of the numerical method; therefore, it is a physical effect.

Assuming that the presence of shock holes is caused by locally subsonic flow approaching the shock is shown to lead to a regime criterion for the 'broken shock' (shock holes do appear) and 'wrinkled shock' (shock holes never appear; the shock maintains its topology at all times) regimes; specifically, an interaction is in the 'broken shock' regime for $M_t \gtrsim 0.6(M-1)$. The factor of 0.6 comes purely from the DNS data; however, we note that this coincides with the value predicted by Donzis (2012*b*) when he assumed a Gaussian pre-shock velocity field.

Acknowledgements

This work was supported by the US Department of Energy under the SciDAC program and by the US Air Force under the Aerothermodynamics and Turbulence program. The computations were run at the US Department of Energy NERSC and ALCF locations under the ERCAP and INCITE programs, respectively.

REFERENCES

AGUI, J. H., BRIASSULIS, G. & ANDREOPOULOS, Y. 2005 Studies of interactions of a propagating shock wave with decaying grid turbulence: velocity and vorticity fields. *J. Fluid Mech.* **524**, 143–195.

BARRE, S., ALEM, D. & BONNET, J. P. 1996 Experimental study of a normal shock/homogeneous turbulence interaction. *AIAA J.* **34** (5), 968–974.

DONZIS, D. A. 2012*a* Amplification factors in shock–turbulence interactions: effect of shock thickness. *Phys. Fluids* **24**, 011705.

DONZIS, D. A. 2012*b* Shock structure in shock–turbulence interactions. *Phys. Fluids* **24**, 126101.

DUCROS, F., LAPORTE, F., SOULERES, T., GUINOT, V., MOINAT, P. & CARUELLE, B. 2000 High-order fluxes for conservative skew-symmetric-like schemes in structured meshes: application to compressible flows. *J. Comput. Phys.* **161**, 114–139.

GRUBE, N. E., TAYLOR, E. M. & PINO MARTÍN, M. 2011 Numerical investigation of shock-wave/isotropic turbulence interaction. In *49th AIAA Aerospace Sciences Meeting*, 4–7 January 2011, Orlando, FL.

HANNAPPEL, R. & FRIEDRICH, R. 1995 Direct numerical simulation of a Mach 2 shock interacting with isotropic turbulence. *Appl. Sci. Res.* **54**, 205–221.

HESSELINK, L. & STURTEVANT, B. 1988 Propagation of weak shocks through a random medium. *J. Fluid Mech.* **196**, 513–553.

JACQUIN, L., CAMBON, C. & BLIN, E. 1993 Turbulence amplification by a shock wave and rapid distortion theory. *Phys. Fluids* **5** (10), 2539–2550.

JAMME, S., CAZALBOU, J.-B., TORRES, F. & CHASSAING, P. 2002 Direct numerical simulation of the interaction between a shock wave and various types of isotropic turbulence. *Flow Turbul. Combust.* **68**, 227–268.

JOHNSEN, E., LARSSON, J., BHAGATWALA, A. V., CABOT, W. H., MOIN, P., OLSSON, B. J., RAWAT, P. S., SHANKAR, S. K., SJÖGREEN, B., YEE, H. C., ZHONG, X. & LELE, S. K. 2010 Assessment of high-resolution methods for numerical simulations of compressible turbulence with shock waves. *J. Comput. Phys.* **229**, 1213–1237.

KELLER, J. & MERZKIRCH, W. 1990 Interaction of a normal shock wave with a compressible turbulent flow. *Exp. Fluids* **8**, 241–248.

KOVASZNAY, L. S. G. 1953 Turbulence in supersonic flow. *J. Aeronaut. Sci.* **20** (10), 657–674 [reprinted 2003 *AIAA J.***41** (7), 219–237].

LARSSON, J. 2009 Blending technique for compressible inflow turbulence: algorithm localization and accuracy assessment. *J. Comput. Phys.* **228**, 933–937.

LARSSON, J. 2010 Effect of shock-capturing errors on turbulence statistics. *AIAA J.* **48** (7), 1554–1557.

LARSSON, J. & GUSTAFSSON, B. 2008 Stability criteria for hybrid difference methods. *J. Comput. Phys.* **227**, 2886–2898.

LARSSON, J. & LELE, S. K. 2009 Direct numerical simulation of canonical shock/turbulence interaction. *Phys. Fluids* **21**, 126101.

LEE, S., LELE, S. K. & MOIN, P. 1993 Direct numerical simulation of isotropic turbulence interacting with a weak shock wave. *J. Fluid Mech.* **251**, 533–562.

LEE, S., LELE, S. K. & MOIN, P. 1994 Corrigendum: direct numerical simulation of isotropic turbulence interacting with a weak shock wave. *J. Fluid Mech.* **264**, 373–374.

LEE, S., LELE, S. K. & MOIN, P. 1997 Interaction of isotropic turbulence with shock waves: effect of shock strength. *J. Fluid Mech.* **340**, 225–247.

LELE, S. K. 1992 Shock-jump relations in a turbulent flow. *Phys. Fluids* **4** (12), 2900–2905.

MAHESH, K., LELE, S. K. & MOIN, P. 1997 The influence of entropy fluctuations on the interaction of turbulence with a shock wave. *J. Fluid Mech.* **334**, 353–379.

PIROZZOLI, S. 2002 Conservative hybrid compact-WENO schemes for shock–turbulence interaction. *J. Comput. Phys.* **178**, 81–117.

RIBNER, H. S. 1953 Convection of a pattern of vorticity through a shock wave. NACA Report 1164.

RIBNER, H. S. 1954 Shock–turbulence interaction and the generation of noise. NACA Report 1233.

SESTERHENN, J., DOHOGNE, J. F. & FRIEDRICH, R. 2005 Direct numerical simulation of the interaction of isotropic turbulence with a shock wave using shock-fitting. *C. R. Méc.* **333**, 87–94.

SINHA, K. 2012 Evolution of enstrophy in shock/homogeneous turbulence interaction. *J. Fluid Mech.* **707**, 74–110.

SINHA, K., MAHESH, K. & CANDLER, G. V. 2003 Modelling shock unsteadiness in shock/turbulence interaction. *Phys. Fluids* **15** (8), 2290–2297.

WILCOX, D. C. 2000 *Turbulence Modelling for CFD*. DCW Industries.

WOUCHUK, J. G., HUETE RUIZ DE LIRA, C. & VELIKOVICH, A. L. 2009 Analytical linear theory for the interaction of a planar shock wave with an isotropic turbulent vorticity field. *Phys. Rev.* E **79**, 066315.